Clinical Applications of Near-infrared Diffuse Correlation Spectroscopy and Tomography for Tissue Blood Flow Monitoring and Imaging

Yu Shang[1], **Ting Li**[2], and **Guoqiang Yu**[3,*]

[1]Key Laboratory of Instrumentation Science & Dynamic Measurement, North University of China, No.3 Xueyuan Road, Taiyuan, Shanxi 030051, China

[2]State Key Lab Elect Thin Film & Integrated Device, University of Electronic Science & Technology of China, Chengdu, Sichuan 610054, China

[3]Department of Biomedical Engineering, University of Kentucky, 514C RMB, 143 Graham Avenue, Lexington, KY 40506-0108, USA

Abstract

Blood flow is one such available observable promoting a wealth of physiological insight both individually and in combination with other metrics. Near-infrared diffuse correlation spectroscopy (DCS) and, to a lesser extent, diffuse correlation tomography (DCT), have increasingly received interest over the past decade as noninvasive methods for tissue blood flow measurements and imaging. DCS/DCT offers several attractive features for tissue blood flow measurements/imaging such as noninvasiveness, portability, high temporal resolution, and relatively large penetration depth (up to several centimeters). This review first introduces the basic principle and instrumentation of DCS/DCT, followed by presenting clinical application examples of DCS/DCT for the diagnosis and therapeutic monitoring of diseases in a variety of organs/tissues including brain, skeletal muscle, and tumor. Clinical study results demonstrate technical versatility of DCS/DCT in providing important information for disease diagnosis and intervention monitoring.

1. Introduction

Near-infrared (NIR) diffuse optical technologies have gained popularity in recent years as simple, fast, continuous, portable, and relatively inexpensive methods for noninvasive quantification of hemodynamics and metabolism in deep tissues up to several centimeters (Vardi and Nini, 2008; Schachner *et al.*, 2008; Bouye *et al.*, 2005; Boas *et al.*, 2001; Ferrari *et al.*, 2011; Jobsis, 1977; Murkin and Arango, 2009; Shuler *et al.*, 2009). One type of NIR technology, namely near-infrared spectroscopy (NIRS) or diffuse optical spectroscopy (DOS), takes advantage of the low absorption spectrum of biological tissues in the NIR range (650–950 nm) and penetrates deep tissues to detect light absorption by oxy-hemoglobin (HbO_2) and deoxy-hemoglobin (Hb) in red blood cells (RBCs) (Kim *et al.*, 2005; Strangman *et al.*, 2003). As a result, oxy-, deoxy-, total- hemoglobin concentrations

*guoqiang.yu@uky.edu.

(i.e., [HbO$_2$], [Hb], and THC) and tissue blood oxygen saturation (StO$_2$) in local tissue microvasculature can be quantified (Liu *et al.*, 1995; Boas *et al.*, 2001; Wolf *et al.*, 2003; Fantini *et al.*, 1995). Over past decades, a variety of NIRS/DOS technologies have been extensively explored to study various diseases affecting blood oxygenation levels in local and regional tissues (Liu *et al.*, 1995; Wolf *et al.*, 2003; Quaresima *et al.*, 2004; Fantini *et al.*, 1995; Patterson *et al.*, 1989; Al-Rawi and Kirkpatrick, 2006). Correspondingly, diffuse optical tomography (DOT) based on NIRS/DOS has also been developed for 3-dimensional (3-D) imaging of oxygenation distributions in organs or regional tissues (Intes *et al.*, 2010; Eggebrecht *et al.*, 2014; Dehghani *et al.*, 2009; Zhang *et al.*, 2013; Arridge and Hebden, 1997; Jermyn *et al.*, 2013).

Another emerging NIR technology, diffuse correlation spectroscopy (DCS), has also been developed to directly measure blood flow variations in deep tissue microvasculature (Boas *et al.*, 1995; Maret and Wolf, 1989; Pine *et al.*, 1988; Yu *et al.*, 2005a; Jaillon *et al.*, 2007; Boas, 1996; Durduran, 2004; Choe, 2005; Zhou, 2007; Irwin, 2011; Gurley, 2012; Cheng, 2013; He, 2015; Dong, 2015). DCS uses *coherent* NIR light to penetrate deep tissues and monitors temporal light intensity fluctuation caused by moving scatterers (primarily RBCs in the microvasculature) to extract a blood flow index (BFI) (Irwin *et al.*, 2011; Cheung *et al.*, 2001). The relative change of blood flow (rBF) is calculated by normalizing BFI to its baseline value before the physiological change occurs. DCS measurements of tissue blood flow changes have been extensively validated against other standards, including power spectral Doppler ultrasound (Yu *et al.*, 2005b), Doppler ultrasound (Buckley *et al.*, 2009; Roche-Labarbe *et al.*, 2010), laser Doppler (Durduran, 2004; Shang *et al.*, 2011a), Xenon computed tomography (Xenon-CT) (Kim *et al.*, 2010), fluorescent microsphere flow measurement (Zhou *et al.*, 2009), and arterial spin labeling magnetic resonance imaging (ASL-MRI) (Yu *et al.*, 2007). In some studies, DCS has been combined with NIRS/DOS in hybrid instruments to simultaneously measure tissue blood flow and oxygenation (Durduran *et al.*, 2004; Yu *et al.*, 2005a; Cheng *et al.*, 2012; Munk *et al.*, 2012; Shang *et al.*, 2012; Gurley *et al.*, 2012), which allows for the derivation of metabolic rate of tissue oxygen consumption.

Despite advances in DCS applicability, there have been limited tomographic imaging realizations. An early contact-measurement based 3-D diffuse correlation tomography (DCT) approach using an optical fiber array was applied to tissue phantoms with a semi-infinite geometry (Boas and Yodh, 1997), but is disadvantaged *in vivo* due to the irregular geometries of biological tissues. A few noncontact-measurement based DCT examinations have been recently conducted to avoid tissue hemodynamic variations induced by the probe compression or the disturbance of sensitive tissue areas (Culver *et al.*, 2003; Huang *et al.*, 2015a; Zhou *et al.*, 2006; Lin *et al.*, 2014; He *et al.*, 2015; Huang *et al.*, 2015b). In these noncontact measurement systems, lenses were positioned between a sample and an optical fiber array connected to the light sources and detection elements. The noncontact DCS/DCT has been successfully applied in examining blood flow distributions in animal models (Zhou *et al.*, 2006; Culver *et al.*, 2003) and human subjects (Li *et al.*, 2013; He *et al.*, 2015; Lin *et al.*, 2012; Huang *et al.*, 2015c; Huang *et al.*, 2015b).

Since NIRS/DOS/DOT technologies for tissue blood oxygenation measurements have been broadly reviewed (Durduran *et al.*, 2010a; Ferrari *et al.*, 2011; Ghosh *et al.*, 2012; Wolf *et al.*, 2007), our review focuses on the DCS/DCT technologies for tissue blood flow measurements in the clinic. We first introduce the principle and instrumentation of DCS/ DCT. We then provide typical clinical examples of DCS/DCT for the diagnosis of diseases and therapeutic monitoring of interventions in a variety of organs/tissues such as brain, skeletal muscle, and tumor. Finally, we highlight the limitations of DCS/DCT and point out future perspectives in technology development and clinical applications.

2. DCS/DCT Methods

2.1 Diffuse Correlation Spectroscopy (DCS)

DCS originates from the concept of "dynamic light scattering (DLS)", a technology that can be used to quantify the motion of moving scatterers in a thin solution through investigating the correlation of light electric field after photons are scattered once by the moving scatterers (i.e., single light scattering) (Brown, 1993; Fletcher, 1976). The extension from single light scattering to multiple light scattering has been explored since 1980s (Maret and Wolf, 1987; Pine *et al.*, 1988; Boas *et al.*, 1995). This extension, called diffusing-wave spectroscopy (DWS) (Pine *et al.*, 1988; Li *et al.*, 2005; Jaillon *et al.*, 2006) or diffuse correlation spectroscopy (DCS) (Cheung *et al.*, 2001; Yu *et al.*, 2005a; Gagnon *et al.*, 2008; Boas and Yodh, 1997; Boas *et al.*, 1995), makes it possible to quantify the motion of moving scatterers in a thick sample, such as red blood cells (RBCs) flowing through biological tissues.

The principle and instrumentation of DCS have been described elsewhere (Boas *et al.*, 1995; Cheung *et al.*, 2001; Durduran and Yodh, 2014; Irwin *et al.*, 2011; Yu, 2012b, a; Yu, 2012c). Briefly, a long-coherence laser delivers NIR light via an optical fiber to the tissue (Fig. 1a). Photons entering into the tissue are either absorbed or more dominantly, scattered by static scatterers (e.g., organelles and mitochondria) and dynamic scatterers (mainly moving RBCs). Due to the scattering effect photons may change directions many times while traveling throughout the tissue, resulting in light diffusion. Only a few photons can eventually reach tissue surface and be collected by a single-mode detector fiber placed millimeters or centimeters away from the source fiber. Photons collected by the detector fiber are detected by a single photon-counting avalanche photodiode (APD) to yield light intensity signals (Fig. 1b).

The detected light intensity fluctuates with time (Fig. 1b), which is caused by the motion of moving scatterers (mainly RBCs) inside the tissue volume measured. To quantify the motion of RBCs (i.e., blood flow) the normalized light intensity temporal autocorrelation function ($g_2(\tau)$) is calculated by a hardware correlator board or a software correlator, which can then be converted to the normalized electric field temporal autocorrelation function ($g_1(\tau)$, Fig. 1c) through the Siegert relation (Rice, 1954):

$$g_2(\vec{r}, \tau) = 1 + \beta |g_1(\vec{r}, \tau)|^2 \quad (1)$$

where τ is the correlation delay time, $\vec{r}$ is the position vector, and β is a parameter which is dependent of laser stability, coherence length, and the number of speckles detected.

The $g_1(\tau)$ can be expressed in an integral form (Boas and Yodh, 1997; Li *et al.*, 2013; Pine *et al.*, 1988; Maret and Wolf, 1987)

$$g_1(\tau) = \frac{\langle E(0) E^*(\tau) \rangle}{\langle |E(0)|^2 \rangle} = \int_0^\infty P(s) \exp(-\frac{1}{3} k_0^2 <\Delta r^2(\tau)> \frac{s}{l^*}) ds \tag{2}$$

Here $E(0)$ and $E^*(\tau)$ are the scattered light electric field at time 0 and its conjugation at time τ, respectively. $P(s)$ is the normalized distribution of detected photon path length s, k_0 is the wave vector magnitude of the light in the medium, and l^* is the photon random-walk step length, which is equal to $1/\mu_s'$ (μ_s' is the medium reduced scattering coefficient).

The unknown $<\Delta r^2(\tau)>$ represents the mean-square-displacement of moving scatterers, which is conventionally difficult to be solved directly using Eq. 2. Alternately, the integral form of autocorrelation function can be converted to a partial differential equation form (Pine *et al.*, 1990). As such, the unnormalized electric field autocorrelation function $G_1(\tau) = <E(0)E^*(\tau)>$ satisfies a correlation diffusion equation (Cheung *et al.*, 2001; Boas and Yodh, 1997)

$$\left(D\nabla^2 - \nu\mu_a - \frac{1}{3}\nu\mu_s' k_0^2 \left\langle \Delta r^2(\tau) \right\rangle \right) G_1(\vec{r}, \tau) = -\nu S(\vec{r}) \tag{3}$$

Here, ν is the light speed in the medium; μ_a is the medium absorption coefficient; $D \approx \nu/3\mu_s'$ is the medium photon diffusion coefficient, and $S(\vec{r})$ is the continuous-wave isotropic source. The form of $<\Delta r^2(\tau)>$ depends on a flow model specifically adopted. For example, a diffuse model, i.e., $<\Delta r^2(\tau)> = 6D_B\tau$, has been found to fit experimental data well over a wide range of different tissues (Cheung *et al.*, 2001; Irwin *et al.*, 2011). Here, D_B is the effective diffusive coefficient. To account for the fact that not all scatterers are "moving" in the tissue, a factor α, representing the ratio of "moving" scatterers to the total number of scatterers, is added to $<\Delta r^2(\tau)>$ (i.e., $<\Delta r^2(\tau)> = 6\alpha D_B\tau$). The combined term, αD_B, is referred to as blood flow index (BFI) in biological tissues. The αD_B can be extracted by fitting the measured autocorrelation function curve to an analytical solution of the correlation diffusion equation (Eq. 3) under certain geometries (e.g., semi-infinite boundary) (Cheung *et al.*, 2001; Dong *et al.*, 2012a; Roche-Labarbe *et al.*, 2010; Irwin *et al.*, 2011).

2.2 Diffuse Correlation Tomography (DCT)

The extension of DCS to DCT is comparable to that of DOS extension to DOT, which images the optical property distribution based on photon diffusion equation and its inverse solutions (i.e., image reconstruction). A DOT instrument typically illuminates tissue and

measures the diffusive light leaving the tissue with multiple sources and detectors on the tissue boundary (Intes *et al.*, 2010; Eggebrecht *et al.*, 2014; Dehghani *et al.*, 2009; Zhang *et al.*, 2013). The diffusive propagation of light in tissue can be characterized with photon diffuse equation and parameterized in terms of the unknown $\mu_a(\vec{r})$ and $\mu'_s(\vec{r})$ at different locations $(\vec{r})$ of the measured tissue volume. One can then "invert" the propagation model to recover these unknown parameters. Imaging with DOT has been described in many papers covering computer simulations, phantom tests, and *in vivo* applications (Franceschini *et al.*, 2006; Durduran *et al.*, 2010a; Eggebrecht *et al.*, 2014; Arridge and Lionheart, 1998; Arridge and Hebden, 1997; Jermyn *et al.*, 2013; Dehghani *et al.*, 2009).

Similarly, DCT requires a large number of sources and detectors to measure autocorrelation functions on the tissue boundary. Early DCT approaches rely on analytical solutions of Eq. 3 with the assumption of simple semi-infinite geometries and/or strict heterogeneities (e.g., spherical anomaly) of tissues (Zhou *et al.*, 2006; Culver *et al.*, 2003), which precludes the transition to complex boundaries and imperfect heterogeneities in realistic tissues.

The finite-element-method (FEM) framework has been applied to model light transport in highly diffuse media to resolve the geometry and heterogeneity limitations for DOS/DOT (Arridge and Lionheart, 1998; Arridge and Hebden, 1997; Eggebrecht *et al.*, 2014; Dehghani *et al.*, 2009; Jermyn *et al.*, 2013). For example, NIRFAST (www.nirfast.org) (Dehghani *et al.*, 2009; Jermyn *et al.*, 2013) and TOAST++ (http://web4.cs.ucl.ac.uk/research/vis/toast/) (Schweiger and Arridge, 2014) are publically available image reconstruction toolboxes based on the diffusive model and FEM for DOT

Exploiting the high mathematical similarity of the forward and inverse problems (e.g., boundary conditions and mathematical assumptions) between DOT and DCT, our group first reported the application of FEM in DCT (Lin *et al.*, 2014; Huang *et al.*, 2015a; He *et al.*, 2015; Huang *et al.*, 2015b). We introduced this concept into the FEM-based light transport and image reconstruction modules in NIRFAST (Dehghani *et al.*, 2009), as a shortcut for FEM implementation of DCT. Specifically, we used the "*effective* $\mu_a(\vec{r})$" (i.e., $\mu_a(\vec{r}) + 2\mu'_s(\vec{r})k_0^2 \Delta\alpha D_B(\vec{r})\tau$) and measured $G_1(\vec{r}, \tau)$ to replace the $\mu_a(\vec{r})$ and photon fluence rate $\Phi(\vec{r}, t)$ respectively in the NIRFAST for the accomplishment of DCT in tissues with complex boundaries (Lin *et al.*, 2014; Huang *et al.*, 2015a; He *et al.*, 2015; Huang *et al.*, 2015b). Computer simulations, phantom tests, and *in-vivo* studies have verified the accuracy of our modifications of NIRFAST adapted for DCT. As a result, the realm of DCT becomes available for comprehensive imaging under complex geometries and heterogeneous optical properties.

2.3 DCS/DCT Instrumentation

Typical DCS/DCT systems are illustrated in Fig. 2. The DCS/DCT systems consist of long-coherence NIR lasers (e.g., 785 nm, Crystalaser, USA), single photon-counting APDs (e.g., SPCM-AQR-12, Perkin Elmer Inc., Canada), and digital correlator boards (e.g., FLEX03LQ, www.correlator.com, USA). A control panel (laptop or desktop) is used to control the DCS/DCT system for data collection and calculation of temporal autocorrelation function via the correlator board. Blood flow index (αD_B) can be extracted by fitting the

measured autocorrelation function curve to an analytical solution of Eq. 3 under certain geometries. In contrast to the portable DCS device (**b**) with a limited number of sources and detectors, the DCT instrument (**c**) has a large number of sources and detectors for 3-D flow imaging.

A variety of fiber-optics probes have been designed for DCS (Fig. 3) and DCT (Fig. 4) measurements in different applications (Huang *et al.*, 2015c; Durduran *et al.*, 2005; Yu *et al.*, 2011; Shang *et al.*, 2011b; Huang *et al.*, 2015b) (see **Section 3**). These probes are connected to the DCS/DCT instruments (Fig. 2) through optical fibers for light delivery and detection. Examples of DCS probes for the studies of brains, skeletal muscles, and tumors are illustrated in Fig. 3a–e, respectively. For instance, a hand-held probe was designed to scan over a breast tumor in both horizontal and vertical directions for diagnostic purpose (Durduran *et al.*, 2005) (Fig. 3d). For the tissues whose shapes promote hemodynamic variations induced by compression or disturb sensitive areas, DCS probes were designed in a noncontact manner (Huang *et al.*, 2015c) (Fig. 3f). In the noncontact measurement design, a lens system with separated source and detector paths was utilized to focus the light from the source and detector fibers on the measured tissue surface. The noncontact DCS (ncDCS) probe was also extended to a noncontact imaging probe head for DCT measurements, which consisted of a linear array of 15 photodetectors and two laser sources connected to a mobile lens-focusing system (Fig. 4) (Lin *et al.*, 2014; He *et al.*, 2015; Huang *et al.*, 2015b). A motorized stage was utilized for automatic scanning (Fig. 4a), enabling large ROI coverage and flexible S-D arrangements without greatly increasing hardware requirements and costs. This new design of noncontact DCT (ncDCT) probe, combined with a novel FEM framework for DCT image reconstruction, has been validated in a tissue-like phantom with anomaly flow contrast design (Fig. 4d) (Lin *et al.*, 2014) and has been applied in detection of breast tumors (He *et al.*, 2015; Huang *et al.*, 2015b). In practice, any innovations adopted in DOS/DOT probes can be adapted for the design of DCS/DCT probes, and a combined probe integrating DOS/DOT and DCS/DCT measurements can be constructed by adding extra optical fibers.

3. Clinical Application Examples

DCS/DCT technologies have been extensively explored to be used in animal models and human subjects for the diagnosis and therapeutic monitoring of diseases in various tissues and organs including brains (Cheng *et al.*, 2014; Hou *et al.*, 2014; Busch *et al.*, 2016a; Kim *et al.*, 2014; Kim *et al.*, 2010; Favilla *et al.*, 2014; Lin *et al.*, 2016; Dehaes *et al.*, 2014; Durduran *et al.*, 2010b; Shang *et al.*, 2011b; Buckley *et al.*, 2013; Zirak *et al.*, 2014), skeletal muscles (Henry *et al.*, 2015; Mesquita *et al.*, 2013; Yu *et al.*, 2005a; Shang *et al.*, 2012; Gurley *et al.*, 2012), and tumors (Chung *et al.*, 2015; Choe *et al.*, 2014; Zhou *et al.*, 2007; Durduran *et al.*, 2005; He *et al.*, 2015; Sunar *et al.*, 2006; Dong *et al.*, 2012b; Dong *et al.*, 2016). Since this review focuses on the clinical applications, only typical clinical examples are presented in the following subsections based on different types of tissues/organs. For more details, readers are encouraged to read primary papers that are cited but not discussed here and to learn from recent reviews (Yu, 2012a; Yu, 2012c; Durduran and Yodh, 2014; Mesquita *et al.*, 2011).

3.1 Brain

3.1.1 Diagnosis of cardio-cerebral diseases—DCS has been explored for the diagnosis and evaluation of cardio-cerebral diseases affecting cerebral blood flow (CBF) in adults, children, and neonates. For example, DCS was utilized to investigate CBF responses in adult patients with cerebral diseases including vasovagal syncope (Cheng et al., 2014), obstructive sleep apnea-hypopnea (Hou *et al.*, 2014; Busch *et al.*, 2016a), traumatic brain injury (Kim *et al.*, 2010; Kim *et al.*, 2014), and ischemic stroke (Durduran *et al.*, 2009; Favilla *et al.*, 2014).

Vasovagal syncope (VVS) is the sudden loss of consciousness, which can be fatal if occurring in public such as driving and flying. In a study of CBF variations to predict VVS (Cheng *et al.*, 2014), a 70-degree head-up-titling (HUT) protocol was applied to 14 healthy adults, and relative changes of CBF (rCBF) to the baseline were continuously monitored using a fiber-optic probe illustrated in Fig. 3a. In addition, relative changes of main artery blood pressure (rMAP) were also continuously monitored using a noninvasive finger sensor (Portapres, FMS Inc., Netherlands). In the subjects having presyncope symptoms during HUT, physiological responses to the tilting were observed to have two stages; while Stage I showed a small changes, Stage II demonstrated a rapid and dramatic decreases in both rCBF and rMAP that were coincided with presyncope symptoms (Fig. 5). On average, rCBF reached the Stage II earlier and decreased larger ($76 \pm 8\%$, from a baseline of 100%) than rMAP ($39 \pm 19\%$, assigning a baseline value of 100%) during presyncope. Moreover, a threshold of ~50% rCBF decline was determined to completely separate the subjects with or without presyncope. This study suggests that continuous monitoring of CBF variations by the portable DCS device may provide predictive information to prevent VVS (e.g., using an automatic feedback to maintain MAP and CBF at normal levels).

Another example of DCS applications is the study of obstructive sleep apnea-hypopnea (OSAH) (Hou *et al.*, 2014), a disease characterized by repetitive pausing of breath resulted from upper airway obstruction during sleep. The impeded airflow during OSAH may cause cerebral ischemia and disturb CBF. Although OSAH can be diagnosed through monitoring of overnight sleep with a polysomnography, evaluation of cerebral ischemia and hypoxia induced by OSAH is not routinely conducted, due to lack of appropriately technologies. Using a dual-wavelength DCS flow-oximeter (Shang *et al.*, 2009), our group conducted continuous and simultaneous measurements of relative changes of CBF, oxy- and deoxy- and total hemoglobin concentrations (rCBF, [HbO_2], [Hb], THC) in adult subjects with OSAH for ~8 hours overnight (Hou *et al.*, 2014). Two fiber-optic probes connected to the DCS flow-oximeter were taped on both sides of the subject's forehead for cerebral monitoring during sleep (illustrated in Fig. 3b). To minimize the disturbance to patients, we remotely operated the optical measurements in a control room and designed special fiber-optic connectors which could easily disconnect the probes when the patient went to bathroom. The results showed that apneic events caused significant variations in rCBF and THC. Moreover, the degrees of these hemodynamic variations were significantly correlated with the severity of OSAH.

Similarly, DCS was also adopted to measure CBF responses to hypercapnia during wakefulness rather than during sleep in children with obstructive sleep syndrome (OSA) and/or snores (Busch *et al.*, 2016a). Both OSA and snore subjects were found to have significant less changes in CBF during hypercapnia than health controls, indicating the diseased-induced blunted brain responses.

DCS was also utilized to monitor CBF variations in adults with traumatic brain injury (Kim et al., 2014; Kim et al., 2010) or ischemic stroke (Favilla *et al.*, 2014; Durduran *et al.*, 2009). In those studies, CBF changes were found to be associated with large variations in cerebral blood pressure induced by physiological manipulations (Kim *et al.*, 2010; Favilla *et al.*, 2014; Durduran *et al.*, 2009), indicating the impairments of cerebral autoregulation to maintain a constant CBF.

In addition to the applications in adults and children, DCS was employed to assess CBF in neonates with malfunctions/defects and during surgical treatments, including those with congenital heart disease (CHD) (Durduran *et al.*, 2010b), hypoxic ischemic encephalopathy (Dehaes et al., 2014), single-ventricle CHD undergoing surgery (Dehaes *et al.*, 2015), as well as the neonates during open heart surgery (Busch *et al.*, 2016b). In those studies, DCS measurements benefited from higher signal-to-noise ratio (SNR) due to the thinner skulls of neonates.

When subjected to a protocol of CO_2 inhalation for inducing hypercapnia (Durduran *et al.*, 2010b), CBF values in neonates with CHD were elevated significantly ($158 \pm 6\%$, assigning a baseline of 100%), which were detectable by both DCS and ASL-MRI measurements. Since complex CHD may lead to impaired cerebral autoregulation and low-baseline CBF, this study explored the potential of DCS for longitudinally probing cerebral defects in critically ill neonates.

Apart from physiological challenging mentioned above, CBF values before and after heart surgeries were measured and compared between the neonates with single-ventricle CHD and healthy controls (Dehaes *et al.*, 2015). The results showed impaired cerebral development in diseased neonates, as characterized by decreased CBF. Furthermore, CBF was continuously monitored during neonatal open heart surgery, an intervention aiming to treat heart defects (Busch *et al.*, 2016b). Significant variations in CBF during deep hypothermia, circulatory arrest, and rewarming were observed, indicating the capability of DCS for cerebral hemodynamic monitoring in a highly challenging clinical environment.

In study of cerebral hemodynamics in premature neonates (Roche-Labarbe *et al.*, 2010), a steady increase (28%, from a baseline of 100%) in CBF was found over the first six weeks of life, indicating that the neonates gained improvements in brain microcirculation since birth. In another study of extremely preterm neonates, the subjects with hemorrhage were found to have lower CBF when compared with those without hemorrhage (Lin *et al.*, 2016). Similarly, lower CBF levels in neonates with hypoxic ischemic encephalopathy were reported, compared to age-matched healthy neonates (Dehaes *et al.*, 2014).

In summary, many cardio-cerebral diseases affect nervous system, cerebral microvasculature, and cerebral oxygen kinetics, leading to abnormality in CBF (Durduran

and Yodh, 2014; Mesquita *et al.*, 2011). Therefore, CBF is considered as an important biomarker of brain health, which links the oxygen demand, supply, and consumption. Continuous measurements of CBF in the clinical setting, however, are not easily achievable due to technology unavailability. DCS offers a continuous, fast, portable, and low-cost tool to noninvasively monitor CBF variations at the bedside of the clinic. Studies presented in this subsection demonstrate that CBF abnormalities are associated with a variety of cerebral diseases. While the explicit relationships between CBF abnormalities and clinical outcomes need to be further investigated, these studies support DCS as a useful tool for the diagnosis of cerebral diseases in adults, children, and neonates.

3.1.2 Therapeutic monitoring of cardio-cerebral diseases—DCS has been used to evaluate the effects of surgical interventions on CBF in adults and infants. Those surgeries included carotid endarterectomy in adults (Shang *et al.*, 2011b), thrombolysis in adults (Zirak *et al.*, 2014), and cardiac surgery in infants (Buckley *et al.*, 2013).

Carotid endarterectomy (CEA) is a surgical intervention to restore the blood supply to brain through removal of the blockage in carotid artery (Shang *et al.*, 2011b). During CEA, some of major vessels are temporarily clamped, causing a shutdown of blood supply to local cerebral tissues. Thus, intraoperative monitoring of CBF variation is particularly important as it permits acute assessment of cerebral hemodynamic level during surgery and post-surgical hemodynamic improvement in the brain. Electroencephalography (EEG) is an often-used technology for cerebral monitoring during CEA, which offers indirect assessment of cerebral ischemia through analysis of brain waves. In a comparison study of EEG and DCS measurements for evaluating cerebral hemodynamic variations during CEA, EEG electrodes were placed all over the scalps of eleven patients undergoing CEA, and two optical probes were taped on both sides of forehead for simultaneous measurements of CBF and cerebral oxygenation. The internal carotid artery (ICA) clamps during CEA resulted in significant CBF decreases ($-24.7 \pm 7.3\%$, assigning a baseline of 100%) at the surgical sides (Fig. 6a). On the other hand, post-CEA CBF values were significantly higher ($+43.2 \pm 16.9\%$, assigning a baseline of 100%) than pre-CEA CBF values. Flow compensation via circle of Willis was also observed at the nonsurgical side (Fig. 6b). CBF responses to ICA clamping were found to be significantly faster, larger, and more sensitive than EEG responses (Fig.7). Simultaneous monitoring of CBF and EEG provided a comprehensive evaluation of cerebral physiological status and showed potential for the adoption of acute interventions (e.g., shunting, medications) during CEA to reduce the risks of severe cerebral ischemia and cerebral hyperperfusion syndrome.

DCS was also applied to a patient with acute ischemic stroke, who received thrombolytic therapy to restore CBF (Zirak *et al.*, 2014). CBF was monitored by DCS throughout the 60-minute thrombolytic therapy. DCS data showed an acute improvement in CBF after thrombolytic therapy, which agreed with the improvement in stroke scale score. This study suggested the potential of continuous DCS monitoring for therapeutic evaluation of acute stroke.

DCS measurements of CBF during interventions were also reported in infants. For example, CBF, cerebral oxygenation, and cerebral oxygen metabolism were continuously monitored

during the period of postoperative neonatal cardiac surgery using a hybrid optical instrument (Buckley *et al.*, 2013). Due to the complicated communications between the cerebral and cardiac vessels, the surgeries on hearts were found to significantly affect cerebral oxygen extraction fraction, but not CBF and cerebral metabolic rate of oxygen consumption.

In summary, many intervention strategies for cardio-cerebral diseases are to restore tissue blood flow. Studies presented in this subsection show high sensitivity of DCS for continuous monitoring of CBF variations during interventions, which holds the potential for dynamic assessment and optimization of cardio-cerebral interventions to maintain CBF in a normal level.

3.2 Skeletal muscle

3.2.1 Diagnosis of muscular diseases—DCS has been adopted to evaluate the vascular diseases affecting skeletal muscle perfusion such as fibromyalgia and peripheral arterial disease (Shang *et al.*, 2012; Mesquita *et al.*, 2013). Evaluation of muscular diseases was often performed in a dynamic manner because those diseases restrict patients from performing leg or arm exercises. Blood flow responses to exercise reflect how skeletal muscles properly perform physiological functions.

In a study of fibromyalgia (FM) (Shang *et al.*, 2012), women with FM were instructed to perform knee extension exercises with steadily increasing intensity. Calf muscle hemodynamics was continuously monitored by a hybrid instrument during exercise using a probe illustrated in Fig. 3c. Results showed that subjects with FM had significantly lower oxygen extraction rate during exercise than healthy controls, and the time of oxygenation recovery were significantly longer. These results suggested an alteration of muscle oxygen utilization in the FM population.

In another study investigating the influence of peripheral arterial disease (PAD) on skeletal muscle hemodynamics (Mesquita *et al.*, 2013), calf blood flow values were found to occur at more depressed levels in PAD population after treadmill and pedal exercises, compared to those in age-matched healthy people. These results indicated adverse impact of PAD on blood flow responses to exercise.

Limitations existed when using DCS techniques to continuously monitor muscle hemodynamic changes *during* exercise, such as the nature of relative measurement (rBF) and the motion artifact induced by the exercise. To overcome these limitations, our group recently created a calibration protocol for absolute flow measurements and a gating algorithm to minimize motion artifacts during exercise (Gurley *et al.*, 2012; Henry *et al.*, 2015). Briefly, a hybrid DCS/NIRS instrument along with a pre-exercise arterial occlusion protocol was utilized to quantify the absolute baseline blood flow value before exercise. The absolute baseline flow value was then used to calibrate the measured rBF during exercise in order to obtain absolute flow measurements over the entire exercising period. Motion artifacts were minimized using a novel dynamometer-based gating algorithm embedded in the DCS control software. Essentially, this software determined muscle contraction status based on signals from the dynamometer and recorded data only when muscle fiber motion was minimal.

The innovative calibration and gating algorithms have been recently applied on patients with FM and compared with age-matched healthy controls. Blood flow responses in forearm muscles to handgrip exercise were continuously monitored and patients with FM exhibited less capability to perform handgrip exercise than healthy controls, evidenced by the weaker blood flow responses during exercise (Fig. 8).

Overall, deficiency of skeletal muscle function may result from mitochondrial dysfunction (Cordero *et al.*, 2010), lower capillary density (Lindh *et al.*, 1995; Morf *et al.*, 2005), reduced capillary permeability (Grassi *et al.*, 1994) and impaired vasodilatory capacity (Kasikcioglu *et al.*, 2006; McIver *et al.*, 2006), all of which are difficult to measure noninvasively. Hybrid DCS/NIRS devices enable noninvasive dynamic quantification of blood flow, blood oxygenation, and oxidative metabolism during exercise, providing unique and comprehensive diagnostic information for skeletal muscle diseases.

3.2.2 Therapeutic monitoring of muscular diseases—A few studies have been reported using DCS to investigate the impacts of surgical interventions on skeletal muscle diseases (Yu *et al.*, 2011; Huang *et al.*, 2015c). For muscular revascularization, ultrasound Doppler is routinely used in surgical rooms to test post-surgical reperfusion in large vessels. However, ultrasound Doppler cannot directly assess the restoration of tissue microcirculation, which is generally the major goal of revascularization.

Using a portable DCS flow-oximeter and the probe illustrated in Fig. 3c (Shang *et al.*, 2009), we continuously monitored calf muscle blood flow variations on twelve human limbs undergoing artery revascularization (Yu *et al.*, 2011). The high sensitivity of DCS in detecting blood flow changes was confirmed through clamping or ballooning on/off the femoral or aorta arteries during surgeries. Furthermore, immediate hyperemia following the release of occlusions and post-surgery flow improvements in calf muscles were observed, indicating the potential of the DCS for objective assessment of revascularization effects.

Another representative application of DCS is the assessment of blood flow in free transfer muscle flaps following salvage surgeries in patients with head and neck cancer. Conventional approaches to evaluate the success of tissue flaps rely on visual examination along with blood flow measurements in large vessels by ultrasound Doppler. DCS offers a tool to directly assess tissue blood flow in peripheral muscle flaps, which is crucial to evaluate the success of surgeries. For intraoperative monitoring of reconstructive flaps, we designed a lens system which focused the sources and detectors on the tissue surface, permitting noncontact measurements of flap blood flow (see Fig. 3f) (Huang *et al.*, 2015c). The noncontact DCS probe was applied to eight free muscle flaps at multiple time points of blood flow measurements during and post the surgical operations. Fig. 9 shows comparison results obtained from seven successful flaps and one unsuccessful flap. Postoperative blood flow values in the successful flaps were significantly higher than the intraoperative baseline values, indicating a gradual recovery of flap vascularity after the tissue transfer. By contrast, postoperative blood flow recovered much less in the unsuccessful flap. Measurement of blood flow recovery after flap anastomosis holds the potential to act early to salvage ischemic flaps.

3.3 Tumor

3.3.1 Diagnosis of tumors—The first translational case of DCS for clinical cancer diagnosis was reported on human breast tumors (Durduran *et al.*, 2005). Through scanning over the breast tumors (n = 5) using a contact optical probe illustrated in Fig. 3d, higher blood flow contrasts were found in malignant (230% by averaging over three subjects) and benign (153% by averaging over two subjects) tumors, respectively, as compared to the surrounding normal tissues (assigning 100%). Similar measurement configuration was thereafter applied to a larger population with breast tumors (n = 32) (Choe *et al.*, 2014), confirming the high blood flow contrasts in breast tumors (225~227% in mean value and 190~270% in 95% confidence intervals).

Moreover, a recent pilot study investigated the correlations between tumor hemodynamic parameters (i.e., blood flow, [HbO_2], [Hb], StO_2, THC) and tumor histopathological biomarkers. Increased blood supply to breast tumors was observed, which agreed with the high expression level of Ki67 nuclei in the confirmed breast tumors (Chung *et al.*, 2015). This study suggested that the macroscopic measurements of tissue hemodynamics could reveal pathological properties of breast cancer in microscopic level.

A significant problem with contact DCS measurements described above is the deformation of soft breast tissue, which may distort blood flow distribution in the soft breast. To solve this problem, noncontact DCS/DCT (ncDCS/ncDCT) systems with unique fiber-optic probes were recently developed enabling fully noncontact measurement/imaging of blood distributions in deep tissue volumes with complex boundaries (Lin *et al.*, 2014; Lin *et al.*, 2012; Li *et al.*, 2013; Huang *et al.*, 2015c; He *et al.*, 2015; Huang *et al.*, 2015b). The noncontact probe was attached to a motorized stage that scanned linearly or rotationally over a ROI (Fig. 4). Fig. 10 shows *in vivo* imaging results from two breast carcinomas. Higher blood flow contrasts (5.9- and 10.9-fold) in the tumor regions compared to the surrounding tissues were observed. The reconstructed locations of the two tumors matched ultrasound imaging results when the tumor was within the sensitivity region of diffuse light. The ncDCT system showed the promise to image blood flow distributions in soft and vulnerable tissues without distorting tissue hemodynamics.

The autonomic growth and spread of tumors are dependent on increased angiogenesis arising from the increased metabolic demand. Since functional alternations in tumors often appear earlier than detectable morphological changes, functional imaging of tumor blood flow by DCT is a new strategy for early cancer diagnosis and localization.

3.3.2 Therapeutic monitoring of tumor treatments—It has been found that the patients with hypoxic tumors show incomplete clinical responses when receiving chemo-radiation therapy that requires tissue oxygen for treatment efficacy (Busch *et al.*, 2000; Carlson, 2006). Many tumors are hypoxic because of abnormal vasculature, malignancy-related anemia, and/or high oxygen consumption by tumor cells. Studies have shown that pretreatment tumor hypoxia is associated with significantly poor responses to the therapy when compared to oxygenated tumors. However, some well-oxygenated tumors failed to respond while some hypoxic tumors responded well, possibly due to the dynamic changes during treatment in tumor oxygen status induced by radiation. Therefore, repeated

monitoring of individual tumor hemodynamic status during therapy may provide predictive information for treatment outcomes.

To date, DCS has been utilized to monitor the tumor hemodynamic responses to chemo-radiation therapy in breast tumors (Zhou *et al.*, 2007) and head/neck tumors (Sunar *et al.*, 2006; Dong *et al.*, 2012b; Dong *et al.*, 2016). In a case study of breast cancer using a hybrid DCS/NIRS device, significant changes in tumor blood flow and blood oxygenation were observed in the first week of chemo-radiation therapy (Zhou *et al.*, 2007).

In another pilot study of head/neck tumors using a hybrid DCS/NIRS instrument, tumor hemodynamic responses in a small group of patients (n = 8) were continually measured once a week over the period of chemo-radiation therapy (Sunar *et al.*, 2006). Tumors exhibited significant dynamic flow and oxygenation changes during the first four weeks of the treatment. This study, however, was limited by the small number of patients examined and only one patient out of 8 showed a partial response to the treatment.

Very recently, our group employed a hybrid DCS/NIRS instrument to continually monitor tumor hemodynamic responses to chemo-radiation therapy for early prediction of treatment outcomes in a relative large patient population with head/neck cancers (Dong *et al.*, 2016). Forty-seven patients were measured once per week over 7 weeks of treatment period to evaluate the hemodynamic status of clinically involved cervical lymph nodes. Patients were classified into two groups: complete response (CR) (n = 29) and incomplete response (IR) (n = 18). Interestingly, tumor hemodynamic responses were found to be associated with clinical outcomes (CR/IR), wherein the associations differed depending on human papillomavirus (HPV-16) status. In HPV-16 positive patients, significantly lower levels in tumor $[HbO_2]$ at weeks 1 to 3, THC at week 3, and StO_2 at week 3 were found in the IR group. In HPV-16 negative patients, significantly higher levels in tumor BFI and $\mu_s{}'$ at week 3 were observed in the IR group. These hemodynamic parameters exhibited significantly high accuracies for early prediction of clinical outcomes, within the first three weeks of therapy, with the areas under the receiver operating characteristic curves (AUCs) ranging from 0.83 to 0.96 (Fig. 11).

Overall, tumor hemodynamic parameters exhibited significantly high accuracies for early prediction of clinical outcomes. Such predications, based on frequent optical measurements, may ultimately be used to optimize individual therapeutic outcomes at an early time of therapy. For example, treatment outcomes may be improved by dynamically promoting oxygenation levels (e.g., hyperbaric oxygen therapy) in HPV-16 positive tumors or inhibiting angiogenesis (e.g., anti-VEGF antibody) in HPV-16 negative tumors.

4. Summary and future perspectives

In contrast to large imaging modalities such as CT, MRI, and PET, optical instruments such as NIRS/DOS/DOT and DCS/DCT are portable, fast, inexpensive, and suitable for continuous measurements at the bedside of clinical settings. NIRS/DOS/DOT techniques have been extensively used to measure tissue oxygenation in the clinic. Compared to NIRS/DOS/DOT, DCS/DCT is a relatively new technique that enables direct measurement

of tissue blood flow. DCS/DCT or hybrid DCS/NIRS is being increasingly employed worldwide in a large variety of clinical contexts for the diagnosis and therapeutic monitoring of various diseases affecting tissue hemodynamics and metabolism. Overall, these pilot clinical studies in relatively small populations have shown the technique's versatility and demonstrated that the method provides new and complementary information about patient pathophysiology in a noninvasive fashion. It should be noticed that DCS/DCT has only been applied to a small population of patients with short measurement time frames (minutes to several weeks). Longitudinal studies in large populations are needed to elucidate potential unresolved technical problems and translate DCS/DCT into the clinic as a routine diagnostic and monitoring tool.

There has been a concern on the physical modeling of blood flow (i.e., the motion of red blood cells) in the microvasculature. It was found that diffusive motion (see Section 2.1) fits the experimental autocorrelation curves rather well over a broad range of tissue types (Durduran, 2004; Zhou, 2007). Intuitively, however, random ballistic flow would be considered as a better model to fit the DCS/DCT data. Modified mixture models were proposed to include both ballistic flow and diffusive motion (Carp *et al.*, 2011; Boas *et al.*, 2016). Experimental data supported the proposed models for capturing the transition from early ballistic to subsequent diffusive motion. Computer simulations on the tissue with varied vessel diameters and spacing showed that the diffusive motion dominates the correlation decay in typical DCS measurements, and the blood flow index is modulated proportionally by the concentration of hemoglobin and the average diameter of blood vessels. Nevertheless, more clinical investigations are needed for accurate extracting of blood flow information in deep tissues.

Some technical issues exist when applying NIR diffuse optical technologies to deep tissues with heterogeneous properties. Since NIRS and DCS techniques rely on the transport of NIR light through top layer tissues (e.g., skin, skull), both methods must account for partial volume contributions from the top layer-structure to the deep tissue signals (e.g., brain, muscle, and tumor). In addition, measurement signal-to-noise ratio (SNR) and penetration depth are two interrelated and important parameters that affect the utility of both DCS and NIRS. Furthermore, most research with DCS reports only relative changes of blood flow index with respect to some baseline condition.

The "partial volume effect" substantially affects the accuracy of DCS measurements, as discussed in literature (Durduran and Yodh, 2014; Yu, 2012a; Strangman *et al.*, 2003). Slab-layered models were proposed to reduce the partial volume effect (Jaillon *et al.*, 2006; Li *et al.*, 2005; Verdecchia *et al.*, 2016). A recently developed method, "Modified Beer-Lambert law for blood flow", has been proved to be effective in pressure modulation experiments to reduce the skin-effect on cerebral blood flow measurements (Baker *et al.*, 2014; Baker *et al.*, 2015). However, those methods ignored the influence of irregular tissue geometries. Recently, we created a new algorithm integrating a linear model of autocorrelation function with the Monte Carlo simulation of photon migrations in heterogeneous tissues with arbitrary geometries for simultaneous extraction of blood flow indices in multiple layered tissues (Shang and Yu, 2014).

Compared to NIRS/DOS/DOT, DCS/DCT measurements have relatively lower SNRs when probing deep tissue blood flow with large S-D separations (e.g., >2.5 mm). This is due to the utilization of single-mode detector fibers with a small core diameter of 5 μm in DCS/DCT measurements to ensure the detection of autocorrelation functions of light intensity. Efforts have been made to improve SNR through the spatial average of multiple autocorrelation functions detected by a detector fiber bundle (Dietsche *et al.*, 2007) or the temporal average of DCS signals obtained by a fast software correlator (Wang *et al.*, 2016).

A potential remedy for the absolute blood flow measurement problem is to calibrate DCS/DCT against a gold standard. As mentioned early, comparison studies in small populations have been done in skeletal muscles, tumors, and brains against other established methods including power spectral Doppler ultrasound (Yu *et al.*, 2005b), Doppler ultrasound (Buckley *et al.*, 2009; Roche-Labarbe *et al.*, 2010), laser Doppler (Durduran, 2004; Shang *et al.*, 2011a), Xenon-CT (Kim *et al.*, 2010), fluorescent microsphere flow measurement (Zhou *et al.*, 2009), and ASL-MRI (Yu *et al.*, 2007). Results from these studies show the promise to obtain absolute flow measurements although further validation works need to be done with different types of tissues in large populations.

DCT/ncDCT enables 3-D imaging of blood flow distributions in deep tissues. While effective, ncDCS/ncDCT employs a limited number of expensive APDs for blood flow detection, leading to low spatiotemporal resolution and high instrument cost (Lin *et al.*, 2014; He *et al.*, 2015; Huang *et al.*, 2015b). With current ncDCT, the ROI must be mechanically scanned for a complete tissue coverage, which can take up to 40 minutes and may result in motion artifacts. To overcome these limitations, we recently developed and tested a non-scanning, noncontact, fast, portable, cost-effective device, namely speckle contrast diffuse correlation tomography (scDCT), for 3-D imaging flow distributions (Huang *et al.*, 2015a; Huang *et al.*, 2016). The scDCT used a charge-coupled-device (CCD) as a 2-D detector array to cover a ROI, thus eliminating the mechanical scanning and consequent problems. Thousands of detectors provided by the CCD significantly improved spatiotemporal resolution and reduced instrument cost/size. The scDCT prototype has been tested using computer simulations and tissue phantoms with anomaly flow contrast design. We are currently translating this novel optical technique to the clinic.

It is well known that many diseases are associated with tissue hypoxia, which is influenced by oxygen supply (i.e., blood flow) and tissue oxygen consumption. Simultaneous measurements of tissue blood flow and blood oxygenation using combined DCS and NIRS instruments enable the evaluation of tissue metabolic rate of oxygen consumption (Durduran *et al.*, 2004; Roche-Labarbe *et al.*, 2010; Lin *et al.*, 2016; Dehaes *et al.*, 2014; Durduran *et al.*, 2010b; Buckley *et al.*, 2013; Henry *et al.*, 2015; Shang *et al.*, 2012; Gurley *et al.*, 2012; Chung *et al.*, 2015). This metabolic parameter is potentially a more direct indicator of tissue metabolic activities, which integrates many factors and provides further insight about tissue pathophysiology. It is expected that with further technology development and more clinical applications, DCS/DCT and hybrid DCS/NIRS technologies will be eventually utilized as routine diagnostic and intervention monitoring tools for clinical investigations of various diseases.

Acknowledgments

References

Al-Rawi PG, Kirkpatrick PJ. Tissue oxygen index - Thresholds for cerebral ischemia using near-infrared spectroscopy. Stroke. 2006; 37:2720–5. [PubMed: 17008623]

Arridge SR, Hebden JC. Optical imaging in medicine: II. Modelling and reconstruction. Phys Med Biol. 1997; 42:841–53. [PubMed: 9172263]

Arridge SR, Lionheart WR. Nonuniqueness in diffusion-based optical tomography. Opt Lett. 1998; 23:882–4. [PubMed: 18087373]

Baker WB, Parthasarathy AB, Busch DR, Mesquita RC, Greenberg JH, Yodh AG. Modified Beer-Lambert law for blood flow. Biomed Opt Express. 2014; 5:4053–75. [PubMed: 25426330]

Baker WB, Parthasarathy AB, Ko TS, Busch DR, Abramson K, Tzeng SY, Mesquita RC, Durduran T, Greenberg JH, Kung DK, Yodh AG. Pressure modulation algorithm to separate cerebral hemodynamic signals from extracerebral artifacts. Neurophotonics. 2015; 2:035004. [PubMed: 26301255]

Boas, DA. Diffuse Photon Probes of Structural and Dynamical Properties of Turbid Media: Theory and Biomedical Applications. University of Pennsylvania; Philadelphia, USA: 1996. p. 1-244.

Boas DA, Campbell LE, Yodh AG. Scattering and imaging with diffusing temporal field correlations. Phys Rev Lett. 1995; 75:1855–8. [PubMed: 10060408]

Boas DA, Gaudette T, Strangman G, Cheng XF, Marota JJA, Mandeville JB. The accuracy of near infrared spectroscopy and imaging during focal changes in cerebral hemodynamics. Neuroimage. 2001; 13:76–90. [PubMed: 11133311]

Boas DA, Sakadzic S, Selb J, Farzam P, Franceschini MA, Carp SA. Establishing the diffuse correlation spectroscopy signal relationship with blood flow. Neurophotonics. 2016; 3:031412. [PubMed: 27335889]

Boas DA, Yodh AG. Spatially varying dynamical properties of turbid media probed with diffusing temporal light correlation. Journal of the Optical Society of America a-Optics Image Science and Vision. 1997; 14:192–215.

Bouye P, Jacquinandi V, Picquet J, Thouveny F, Liagre J, Leftheriotis G, Saumet JL, Abraham P. Near-infrared spectroscopy and transcutaneous oxygen pressure during exercise to detect arterial ischemia at the buttock level: Comparison with arteriography. J Vasc Surg. 2005; 41:994–9. [PubMed: 15944599]

Brown, W. Dynamic Light Scattering: The Method and Some Applications. Clarendon; New York: 1993.

Buckley EM, Cook NM, Durduran T, Kim MN, Zhou C, Choe R, Yu G, Shultz S, Sehgal CM, Licht DJ, Arger PH, Putt ME, Hurt H, Yodh AG. Cerebral hemodynamics in preterm infants during positional intervention measured with diffuse correlation spectroscopy and transcranial Doppler ultrasound. Opt Express. 2009; 17:12571–81. [PubMed: 19654660]

Buckley EM, Lynch JM, Goff DA, Schwab PJ, Baker WB, Durduran T, Busch DR, Nicolson SC, Montenegro LM, Naim MY, Xiao R, Spray TL, Yodh AG, Gaynor JW, Licht DJ. Early postoperative changes in cerebral oxygen metabolism following neonatal cardiac surgery: Effects of surgical duration. Journal of Thoracic and Cardiovascular Surgery. 2013; 145:196–205. [PubMed: 23111021]

Busch DR, Lynch JM, Winters ME, McCarthy AL, Newland JJ, Ko T, Cornaglia MA, Radcliffe J, McDonough JM, Samuel J, Matthews E, Xiao R, Yodh AG, Marcus CL, Licht DJ, Tapia IE. Cerebral Blood Flow Response to Hypercapnia in Children with Obstructive Sleep Apnea Syndrome. Sleep. 2016a; 39:209–16. [PubMed: 26414896]

Busch DR, Rusin CG, Miller-Hance W, Kibler K, Baker WB, Heinle JS, Fraser CD, Yodh AG, Licht DJ, Brady KM. Continuous cerebral hemodynamic measurement during deep hypothermic circulatory arrest. Biomed Opt Express. 2016b; 7:3461–70. [PubMed: 27699112]

Busch TM, Hahn SM, Evans SM, Koch CJ. Depletion of tumor oxygenation during photodynamic therapy: detection by the hypoxia marker EF3 [2-(2-nitroimidazol-1[H]-yl)-N-(3,3,3-trifluoropropyl)acetamide]. Cancer Res. 2000; 60:2636–42. [PubMed: 10825135]

Carlson, DJ. School of Health Sciences. Purdue University; West Lafayette, IN, USA: 2006. Mechanisms of Intrinsic Radiation Sensitivity: The Effects of DNA Damage Repair, Oxygen, and Radiation Quality.

Carp SA, Roche-Labarbe N, Franceschini MA, Srinivasan VJ, Sakadzic S, Boas DA. Due to intravascular multiple sequential scattering, Diffuse Correlation Spectroscopy of tissue primarily measures relative red blood cell motion within vessels. Biomed Opt Express. 2011; 2:2047–54. [PubMed: 21750779]

Cheng, R. Noninvasive near-infrared diffuse optical monitoring of cerebral hemodynamics and autoregulation. University of Kentucky; Lexington, Kentucky, USA: 2013. p. 1-121.

Cheng R, Shang Y, Hayes D, Saha SP, Yu G. Noninvasive optical evaluation of spontaneous low frequency oscillations in cerebral hemodynamics. Neuroimage. 2012; 62:1445–54. [PubMed: 22659481]

Cheng R, Shang Y, Wang SQ, Evans JM, Rayapati A, Randall DC, Yu G. Near-infrared diffuse optical monitoring of cerebral blood flow and oxygenation for the prediction of vasovagal syncope. J Biomed Opt. 2014; 19:017001.

Cheung C, Culver JP, Takahashi K, Greenberg JH, Yodh AG. In vivo cerebrovascular measurement combining diffuse near-infrared absorption and correlation spectroscopies. Phys Med Biol. 2001; 46:2053–65. [PubMed: 11512610]

Choe, R. Diffuse Optical Tomography and Spectroscopy of Breast Cancer and Fetal Brain. University of Pennsylvania; Philadelphia, USA: 2005. p. 1-226.

Choe R, Putt ME, Carlile PM, Durduran T, Giammarco JM, Busch DR, Jung KW, Czerniecki BJ, Tchou J, Feldman MD, Mies C, Rosen MA, Schnall MD, DeMichele A, Yodh AG. Optically Measured Microvascular Blood Flow Contrast of Malignant Breast Tumors. Plos One. 2014; 9:e99683. [PubMed: 24967878]

Chung SH, Feldman MD, Martinez D, Kim H, Putt ME, Busch DR, Tchou J, Czerniecki BJ, Schnall MD, Rosen MA, DeMichele A, Yodh AG, Choe R. Macroscopic optical physiological parameters correlate with microscopic proliferation and vessel area breast cancer signatures. Breast Cancer Res. 2015; 17:72. [PubMed: 26013572]

Cordero MD, De Miguel M, Fernandez AMM, Lopez IMC, Maraver JG, Cotan D, Izquierdo LG, Bonal P, Campa F, Bullon P, Navas P, Alcazar JAS. Mitochondrial dysfunction and mitophagy activation in blood mononuclear cells of fibromyalgia patients: implications in the pathogenesis of the disease. Arthritis Res Ther. 2010; 12:R17. [PubMed: 20109177]

Culver JP, Durduran T, Furuya T, Cheung C, Greenberg JH, Yodh AG. Diffuse optical tomography of cerebral blood flow, oxygenation, and metabolism in rat during focal ischemia. J Cereb Blood Flow Metab. 2003; 23:911–24. [PubMed: 12902835]

Dehaes M, Aggarwal A, Lin PY, Fortuno CR, Fenoglio A, Roche-Labarbe N, Soul JS, Franceschini MA, Grant PE. Cerebral oxygen metabolism in neonatal hypoxic ischemic encephalopathy during and after therapeutic hypothermia. J Cereb Blood Flow Metab. 2014; 34:87–94. [PubMed: 24064492]

Dehaes M, Cheng HH, Buckley EM, Lin PY, Ferradal SL, Williams K, Vyas R, Hagan K, Wigmore D, McDavitt E, Soul JS, Franceschini MA, Newburger JW, Grant PE. Perioperative cerebral hemodynamics and oxygen metabolism in neonates with single-ventricle physiology. Biomed Opt Express. 2015; 6:4749–67. [PubMed: 26713191]

Dehghani H, Eames ME, Yalavarthy PK, Davis SC, Srinivasan S, Carpenter CM, Pogue BW, Paulsen KD. Near infrared optical tomography using NIRFAST: Algorithm for numerical model and image reconstruction. Commun Numer Meth En. 2009; 25:711–32.

Dietsche G, Ninck M, Ortolf C, Li J, Jaillon F, Gisler T. Fiber-based multispeckle detection for time-resolved diffusing-wave spectroscopy: characterization and application to blood flow detection in deep tissue. Appl Optics. 2007; 46:8506–14.

Dong J, Bi RZ, Ho JH, Thong PSP, Soo KC, Lee K. Diffuse correlation spectroscopy with a fast Fourier transform-based software autocorrelator. J Biomed Opt. 2012a; 17:097004.

Dong, L. Diffuse optical measurements of head and neck tumor hemodynamics for early prediction of chemo-radiation therapy outcomes. University of Kentucky; Lexington, Kentucky, USA: 2015. p. 1-117.

Dong L, Kudrimoti M, Cheng R, Shang Y, Johnson EL, Stevens SD, Shelton BJ, Yu G. Noninvasive diffuse optical monitoring of head and neck tumor blood flow and oxygenation during radiation delivery. Biomed Opt Express. 2012b; 3:259–72. [PubMed: 22312579]

Dong L, Kudrimot M, Irwin D, Chen L, Kumar S, Shang Y, Huang C, Johnson EL, Stevens SD, Shelton BJ, Yu G. Diffuse optical measurements of head and neck tumor hemodynamics for early prediction of chemo-radiation therapy outcomes. J Biomed Opt. 2016; 21:085004.

Durduran, T. Non-invasive measurements of tissue hemodynamics with hybrid diffuse optical methods. University of Pennsylvania; Philadelphia, USA: 2004. p. 1-208.

Durduran T, Choe R, Baker WB, Yodh AG. Diffuse optics for tissue monitoring and tomography. Rep Prog Phys. 2010a; 73:076701. [PubMed: 26120204]

Durduran T, Choe R, Yu G, Zhou C, Tchou JC, Czerniecki BJ, Yodh AG. Diffuse optical measurement of blood flow in breast tumors. Opt Lett. 2005; 30:2915–7. [PubMed: 16279468]

Durduran T, Yodh AG. Diffuse correlation spectroscopy for non-invasive, micro-vascular cerebral blood flow measurement. Neuroimage. 2014; 85:51–63. [PubMed: 23770408]

Durduran T, Yu G, Burnett MG, Detre JA, Greenberg JH, Wang JJ, Zhou C, Yodh AG. Diffuse optical measurement of blood flow, blood oxygenation, and metabolism in a human brain during sensorimotor cortex activation. Opt Lett. 2004; 29:1766–8. [PubMed: 15352363]

Durduran T, Zhou C, Edlow BL, Yu G, Choe R, Kim MN, Cucchiara BL, Putt ME, Shah Q, Kasner SE, Greenberg JH, Yodh AG, Detre JA. Transcranial optical monitoring of cerebrovascular hemodynamics in acute stroke patients. Opt Express. 2009; 17:3884–902. [PubMed: 19259230]

Durduran T, Zhou CA, Buckley EM, Kim MN, Yu G, Choe R, Gaynor JW, Spray TL, Durning SM, Mason SE, Montenegro LM, Nicolson SC, Zimmerman RA, Putt ME, Wang JJ, Greenberg JH, Detre JA, Yodh AG, Licht DJ. Optical measurement of cerebral hemodynamics and oxygen metabolism in neonates with congenital heart defects. J Biomed Opt. 2010b; 15:037004. [PubMed: 20615033]

Eggebrecht AT, Ferradal SL, Robichaux-Viehoever A, Hassanpour MS, Dehghani H, Snyder AZ, Hershey T, Culver JP. Mapping distributed brain function and networks with diffuse optical tomography. Nat Photonics. 2014; 8:448–54. [PubMed: 25083161]

Fantini S, Franceschinifantini MA, Maier JS, Walker SA, Barbieri B, Gratton E. Frequency-Domain Multichannel Optical-Detector for Noninvasive Tissue Spectroscopy and Oximetry. Optical Engineering. 1995; 34:32–42.

Favilla CG, Mesquita RC, Mullen M, Durduran T, Lu XP, Kim MN, Minkoff DL, Kasner SE, Greenberg JH, Yodh AG, Detre JA. Optical Bedside Monitoring of Cerebral Blood Flow in Acute Ischemic Stroke Patients During Head-of-Bed Manipulation. Stroke. 2014; 45:1269–74. [PubMed: 24652308]

Ferrari M, Muthalib M, Quaresima V. The use of near-infrared spectroscopy in understanding skeletal muscle physiology: recent developments. Philosophical Transactions of the Royal Society a-Mathematical Physical and Engineering Sciences. 2011; 369:4577–90.

Fletcher GC. Dynamic light scattering from collagen solutions. I Translational diffusion coefficient and aggregation effects. Biopolymers. 1976; 15:2201–17. [PubMed: 990403]

Franceschini MA, Joseph DK, Huppert TJ, Diamond SG, Boas DA. Diffuse optical imaging of the whole head. J Biomed Opt. 2006; 11:054007. [PubMed: 17092156]

Gagnon L, Desjardins M, Jehanne-Lacasse J, Bherer L, Lesage F. Investigation of diffuse correlation spectroscopy in multi-layered media including the human head. Opt Express. 2008; 16:15514–30. [PubMed: 18825190]

Ghosh A, Elwell C, Smith M. Cerebral Near-Infrared Spectroscopy in Adults: A Work in Progress. Anesth Analg. 2012; 115:1373–83. [PubMed: 23144435]

Grassi W, Core P, Carlino G, Salaffi F, Cervini C. Capillary-Permeability in Fibromyalgia. Journal of Rheumatology. 1994; 21:1328–31. [PubMed: 7966078]

Gurley, K. Use of hybrid diffuse optical spectroscopies in continuous monitoring of blood flow, blood oxygenation and oxygen consumption rate in exercising skeletal muscle. University of Kentucky; Lexington, Kentucky, USA: 2012. p. 1-81.

Gurley K, Shang Y, Yu G. Noninvasive optical quantification of absolute blood flow, blood oxygenation, and oxygen consumption rate in exercising skeletal muscle. J Biomed Opt. 2012; 17:075010. [PubMed: 22894482]

He, L. Noncontact diffuse correlation tomography of breast tumor. University of Kentucky; Lexington, Kentucky, USA: 2015. p. 1-126.

He L, Lin Y, Huang C, Irwin D, Szabunio MM, Yu G. Noncontact diffuse correlation tomography of human breast tumor. J Biomed Opt. 2015; 20:86003. [PubMed: 26259706]

Henry B, Zhao MJ, Shang Y, Uhl T, Thomas DT, Xenos ES, Saha SP, Yu G. Hybrid diffuse optical techniques for continuous hemodynamic measurement in gastrocnemius during plantar flexion exercise. J Biomed Opt. 2015; 20:125006. [PubMed: 26720871]

Hou Y, Shang Y, Cheng R, Zhao Y, Qin Y, Kryscio R, Rayapati A, Hayes D, Yu G. Obstructive sleep apnea-hypopnea results in significant variations in cerebral hemodynamics detected by diffuse optical spectroscopies. Physiol Meas. 2014; 35:2135–48. [PubMed: 25243760]

Huang C, Irwin D, Lin Y, Shang Y, He L, Kong WK, Luo J, Yu G. Speckle contrast diffuse correlation tomography of complex turbid medium flow. Med Phys. 2015a; 42:4000–6. [PubMed: 26133600]

Huang C, Lin Y, He L, Irwin D, Szabunio MM, Yu G. Alignment of sources and detectors on breast surface for noncontact diffuse correlation tomography of breast tumors. Appl Optics. 2015b; 54:8808–16.

Huang C, Radabaugh JP, Aouad RK, Lin Y, Gal TJ, Patel AB, Valentino J, Shang Y, Yu G. Noncontact diffuse optical assessment of blood flow changes in head and neck free tissue transfer flaps. J Biomed Opt. 2015c; 20:075008. [PubMed: 26187444]

Huang C, Seong M, Morgan JP, Mazdeyasna S, Kim JG, Hastings JT, Yu G. A low-cost compact diffuse speckle contrast flowmeter using small laser diode and bare charge-coupled-device. J Biomed Opt. 2016; 21:080501.

Intes X, Chen J, Venugopal V, Lesage F. Time-resolved diffuse optical tomography with patterned-light illumination and detection. Opt Lett. 2010; 35:2121–3. [PubMed: 20596166]

Irwin, D. Influence of tissue absorption and scattering on diffuse correlation spectroscopy blood flow measurement. University of Kentucky; Lexington, Kentucky, USA: 2011. p. 1-68.

Irwin D, Dong L, Shang Y, Cheng R, Kudrimoti M, Stevens SD, Yu G. Influences of tissue absorption and scattering on diffuse correlation spectroscopy blood flow measurements. Biomed Opt Express. 2011; 2:1969–85. [PubMed: 21750773]

Jaillon F, Li J, Dietsche G, Elbert T, Gisler T. Activity of the human visual cortex measured non-invasively by diffusing-wave spectroscopy. Opt Express. 2007; 15:6643–50. [PubMed: 19546974]

Jaillon F, Skipetrov SE, Li J, Dietsche G, Maret G, Gisler T. Diffusing-wave spectroscopy from head-like tissue phantoms: influence of a non-scattering layer. Opt Express. 2006; 14:10181–94. [PubMed: 19529414]

Jermyn M, Ghadyani H, Mastanduno MA, Turner W, Davis SC, Dehghani H, Pogue BW. Fast segmentation and high-quality three-dimensional volume mesh creation from medical images for diffuse optical tomography. J Biomed Opt. 2013; 18:86007. [PubMed: 23942632]

Jobsis FF. Noninvasive, infrared monitoring of cerebral and myocardial oxygen sufficiency and circulatory parameters. Science. 1977; 198:1264–7. [PubMed: 929199]

Kasikcioglu E, Dinler M, Berker E. Reduced tolerance of exercise in fibromyalgia may be a consequence of impaired microcirculation initiated by deficient action of nitric oxide. Medical Hypotheses. 2006; 66:950–2. [PubMed: 16412581]

Kim JG, Xia MN, Liu HL. Extinction coefficients of hemoglobin for near-infrared spectroscopy of tissue. IEEE Eng Med Biol Mag. 2005; 24:118–21. [PubMed: 15825855]

Kim MN, Durduran T, Frangos S, Edlow BL, Buckley EM, Moss HE, Zhou C, Yu G, Choe R, Maloney-Wilensky E, Wolf RL, Grady MS, Greenberg JH, Levine JM, Yodh AG, Detre JA, Kofke WA. Noninvasive measurement of cerebral blood flow and blood oxygenation using near-infrared and diffuse correlation spectroscopies in critically brain-Injured adults. Neurocrit Care. 2010; 12:173–80. [PubMed: 19908166]

Kim MN, Edlow BL, Durduran T, Frangos S, Mesquita RC, Levine JM, Greenberg JH, Yodh AG, Detre JA. Continuous Optical Monitoring of Cerebral Hemodynamics During Head-of-Bed Manipulation in Brain-Injured Adults. Neurocrit Care. 2014; 20:443–53. [PubMed: 23653267]

Li J, Dietsche G, Iftime D, Skipetrov SE, Maret G, Elbert T, Rockstroh B, Gisler T. Noninvasive detection of functional brain activity with near-infrared diffusing-wave spectroscopy. J Biomed Opt. 2005; 10:44002. [PubMed: 16178636]

Li T, Lin Y, Shang Y, He L, Huang C, Szabunio M, Yu G. Simultaneous measurement of deep tissue blood flow and oxygenation using noncontact diffuse correlation spectroscopy flow-oximeter. Sci Rep. 2013; 3:1358. [PubMed: 23446991]

Lin PY, Hagan K, Fenoglio A, Grant PE, Franceschini MA. Reduced cerebral blood flow and oxygen metabolism in extremely preterm neonates with low-grade germinal matrix-intraventricular hemorrhage. Sci Rep. 2016; 6:25903. [PubMed: 27181339]

Lin Y, He L, Shang Y, Yu G. Noncontact diffuse correlation spectroscopy for noninvasive deep tissue blood flow measurement. J Biomed Opt. 2012; 17:010502. [PubMed: 22352631]

Lin Y, Huang C, Irwin D, He L, Shang Y, Yu G. Three-dimensional flow contrast imaging of deep tissue using noncontact diffuse correlation tomography. Applied Physics Letters. 2014; 104:121103. [PubMed: 24737919]

Lindh M, Johansson G, Hedberg M, Henning GB, Grimby G. Muscle-Fiber Characteristics, Capillaries and Enzymes in Patients with Fibromyalgia and Controls. Scandinavian Journal of Rheumatology. 1995; 24:34–7. [PubMed: 7863276]

Liu H, Boas DA, Zhang Y, Yodh AG, Chance B. Determination of optical properties and blood oxygenation in tissue using continuous NIR light. Phys Med Biol. 1995; 40:1983–93. [PubMed: 8587945]

Maret G, Wolf PE. Multiple Light-Scattering from Disordered Media - the Effect of Brownian-Motion of Scatterers. Zeitschrift Fur Physik B-Condensed Matter. 1987; 65:409–13.

Maret G, Wolf PE. Multiple Light-Scattering - Weak Localization and Dynamic Fluctuations. Physica Scripta. 1989; T29:223–5.

McIver KL, Evans C, Kraus RM, Ispas L, Sciotti VM, Hickner RC. NO-mediated alterations in skeletal muscle nutritive blood flow and lactate metabolism in fibromyalgia. Pain. 2006; 120:161–9. [PubMed: 16376018]

Mesquita RC, Durduran T, Yu G, Buckley EM, Kim MN, Zhou C, Choe R, Sunar U, Yodh AG. Direct measurement of tissue blood flow and metabolism with diffuse optics. Philosophical Transactions of the Royal Society a-Mathematical Physical and Engineering Sciences. 2011; 369:4390–406.

Mesquita RC, Putt M, Chandra M, Yu G, Xing XM, Han SW, Lech G, Shang Y, Durduran T, Zhou C, Yodh AG, Mohler ER. Diffuse optical characterization of an exercising patient group with peripheral artery disease. J Biomed Opt. 2013; 18:57007. [PubMed: 23708193]

Morf S, Amann-Vesti B, Forster A, Franzeck UK, Koppensteiner R, Uebelhart D, Sprott H. Microcirculation abnormalities in patients with fibromyalgia - measured by capillary microscopy and laser fluxmetry. Arthritis Res Ther. 2005; 7:R209–R16. [PubMed: 15743467]

Munk N, Symons B, Shang Y, Cheng R, Yu G. Noninvasively measuring the hemodynamic effects of massage on skeletal muscle: A novel hybrid near-infrared diffuse optical instrument. Journal of Bodywork and Movement Therapies. 2012; 16:22–8. [PubMed: 22196423]

Murkin JM, Arango M. Near-infrared spectroscopy as an index of brain and tissue oxygenation. British Journal of Anaesthesia. 2009; 103:i3–i13. (BJA/PGA Supplement). [PubMed: 20007987]

Patterson MS, Chance B, Wilson BC. Time resolved reflectance and transmittance for the non-invasive measurement of tissue optical properties. Appl Opt. 1989; 28:2331–6. [PubMed: 20555520]

Pine DJ, Weitz DA, Chaikin PM, Herbolzheimer E. Diffusing-Wave Spectroscopy. Phys Rev Lett. 1988; 60:1134–7. [PubMed: 10037950]

Pine DJ, Weitz DA, Zhu JX, Herbolzheimer E. Diffusing-Wave Spectroscopy - Dynamic Light-Scattering in the Multiple-Scattering Limit. Journal De Physique. 1990; 51:2101–27.

Quaresima V, Ferrari M, Franceschini MA, Hoimes ML, Fantini S. Spatial distribution of vastus lateralis blood flow and oxyhemoglobin saturation measured at the end of isometric quadriceps contraction by multichannel near-infrared spectroscopy. J Biomed Opt. 2004; 9:413–20. [PubMed: 15065910]

Rice, SO. Mathematical analysis of random noise. In: Wax, N., editor. Noise and Stochastic Processes. Dover; New York: 1954. p. 133

Roche-Labarbe N, Carp SA, Surova A, Patel M, Boas DA, Grant RE, Franceschini MA. Noninvasive optical measures of CBV, StO(2), CBF Index, and rCMRO(2) in human premature neonates' brains in the first six weeks of life. Hum Brain Mapp. 2010; 31:341–52. [PubMed: 19650140]

Schachner T, Bonaros N, Bonatti J, Kolbitsch C. Near infrared spectroscopy for controlling the quality of distal leg perfusion in remote access cardiopulmonary bypass. Eur J Cardiothorac Surg. 2008; 34:1253–4. [PubMed: 18835786]

Schweiger M, Arridge S. The Toast plus plus software suite for forward and inverse modeling in optical tomography. J Biomed Opt. 2014:19.

Shang Y, Chen L, Toborek M, Yu G. Diffuse optical monitoring of repeated cerebral ischemia in mice. Opt Express. 2011a; 19:20301–15. [PubMed: 21997041]

Shang Y, Cheng R, Dong L, Ryan SJ, Saha SP, Yu G. Cerebral monitoring during carotid endarterectomy using near-infrared diffuse optical spectroscopies and electroencephalogram. Phys Med Biol. 2011b; 56:3015–32. [PubMed: 21508444]

Shang Y, Gurley K, Symons B, Long D, Srikuea R, Crofford LJ, Peterson CA, Yu G. Noninvasive optical characterization of muscle blood flow, oxygenation, and metabolism in women with fibromyalgia. Arthritis Res Ther. 2012; 14:R236. [PubMed: 23116302]

Shang Y, Yu G. A Nth-order linear algorithm for extracting diffuse correlation spectroscopy blood flow indices in heterogeneous tissues. Applied Physics Letters. 2014:105.

Shang Y, Zhao Y, Cheng R, Dong L, Irwin D, Yu G. Portable optical tissue flow oximeter based on diffuse correlation spectroscopy. Opt Lett. 2009; 34:3556–8. [PubMed: 19927209]

Shuler MS, Reisman WM, Whitesides TE, Kinsey TL, Hammerberg EM, Davila MG, Moore TJ. Near-Infrared Spectroscopy in Lower Extremity Trauma. Journal of Bone and Joint Surgery-American Volume. 2009; 91A:1360–8.

Strangman G, Franceschini MA, Boas DA. Factors affecting the accuracy of near-infrared spectroscopy concentration calculations for focal changes in oxygenation parameters. Neuroimage. 2003; 18:865–79. [PubMed: 12725763]

Sunar U, Quon H, Durduran T, Zhang J, Du J, Zhou C, Yu G, Choe R, Kilger A, Lustig R, Loevner L, Nioka S, Chance B, Yodh AG. Noninvasive diffuse optical measurement of blood flow and blood oxygenation for monitoring radiation therapy in patients with head and neck tumors: a pilot study. J Biomed Opt. 2006; 11:064021. [PubMed: 17212544]

Vardi M, Nini A. Near-infrared spectroscopy for evaluation of peripheral vascular disease. A systematic review of literature. Eur J Vasc Endovasc Surg. 2008; 35:68–74. [PubMed: 17919945]

Verdecchia K, Diop M, Lee A, Morrison LB, Lee TY, St Lawrence K. Assessment of a multi-layered diffuse correlation spectroscopy method for monitoring cerebral blood flow in adults. Biomed Opt Express. 2016; 7:3659–74. [PubMed: 27699127]

Wang DT, Parthasarathy AB, Baker WB, Gannon K, Kavuri V, Ko T, Schenkel S, Li Z, Li ZR, Mullen MT, Detre JA, Yodh AG. Fast blood flow monitoring in deep tissues with real-time software correlators. Biomed Opt Express. 2016; 7:776–97. [PubMed: 27231588]

Wolf M, Ferrari M, Quaresima V. Progress of near-infrared spectroscopy and topography for brain and muscle clinical applications. J Biomed Opt. 2007; 12:062104. [PubMed: 18163807]

Wolf M, Franceschini MA, Paunescu LA, Toronov V, Michalos A, Wolf U, Gratton E, Fantini S. Absolute frequency-domain pulse oximetry of the brain: methodology and measurements. Adv Exp Med Biol. 2003; 530:61–73. [PubMed: 14562705]

Yu G. Diffuse Correlation Spectroscopy (DCS): A Diagnostic Tool for Assessing Tissue Blood Flow in Vascular-Related Diseases and Therapies. Current Medical Imaging Reviews. 2012a; 8:194–210.

Yu G. Near-infrared diffuse correlation spectroscopy (DCS) for assessing deep tissue blood flow. Anatomy and Physiology. 2012b; 2:1000e115.

Yu G. Near-infrared diffuse correlation spectroscopy in cancer diagnosis and therapy monitoring. J Biomed Opt. 2012c; 17:010901. [PubMed: 22352633]

Yu G, Durduran T, Lech G, Zhou C, Chance B, Mohler ER, Yodh AG. Time-dependent blood flow and oxygenation in human skeletal muscles measured with noninvasive near-infrared diffuse optical spectroscopies. J Biomed Opt. 2005a; 10:024027. [PubMed: 15910100]

Yu G, Durduran T, Zhou C, Wang HW, Putt ME, Saunders HM, Sehgal CM, Glatstein E, Yodh AG, Busch TM. Noninvasive monitoring of murine tumor blood flow during and after photodynamic therapy provides early assessment of therapeutic efficacy. Clin Cancer Res. 2005b; 11:3543–52. [PubMed: 15867258]

Yu G, Floyd TF, Durduran T, Zhou C, Wang JJ, Detre JA, Yodh AG. Validation of diffuse correlation spectroscopy for muscle blood flow with concurrent arterial spin labeled perfusion MRI. Opt Express. 2007; 15:1064–75. [PubMed: 19532334]

Yu G, Shang Y, Zhao Y, Cheng R, Dong L, Saha SP. Intraoperative evaluation of revascularization effect on ischemic muscle hemodynamics using near-infrared diffuse optical spectroscopies. J Biomed Opt. 2011; 16:027004. [PubMed: 21361707]

Zhang W, Gao F, Wu LH, Ma WJ, Lu YM, Zhao HJ. A time-domain diffuse fluorescence and optical tomography system for breast tumor diagnosis. J Infrared Millim W. 2013; 32:181–6.

Zhou, C. In-Vivo Optical Imaging and Spectroscopy of Cerebral Hemodynamics. University of Pennsylvania; Philadelphia, USA: 2007. p. 1-325.

Zhou C, Choe R, Shah N, Durduran T, Yu G, Durkin A, Hsiang D, Mehta R, Butler J, Cerussi A, Tromberg BJ, Yodh AG. Diffuse optical monitoring of blood flow and oxygenation in human breast cancer during early stages of neoadjuvant chemotherapy. J Biomed Opt. 2007; 12:051903. [PubMed: 17994886]

Zhou C, Eucker SA, Durduran T, Yu G, Ralston J, Friess SH, Ichord RN, Margulies SS, Yodh AG. Diffuse optical monitoring of hemodynamic changes in piglet brain with closed head injury. J Biomed Opt. 2009; 14:034015. [PubMed: 19566308]

Zhou C, Yu G, Furuya D, Greenberg JH, Yodh AG, Durduran T. Diffuse optical correlation tomography of cerebral blood flow during cortical spreading depression in rat brain. Opt Express. 2006; 14:1125–44. [PubMed: 19503435]

Zirak P, Delgado-Mederos R, Dinia L, Carrera D, Marti-Fabregas J, Durduran T. Transcranial diffuse optical monitoring of microvascular cerebral hemodynamics after thrombolysis in ischemic stroke. J Biomed Opt. 2014; 19:18002. [PubMed: 24413455]
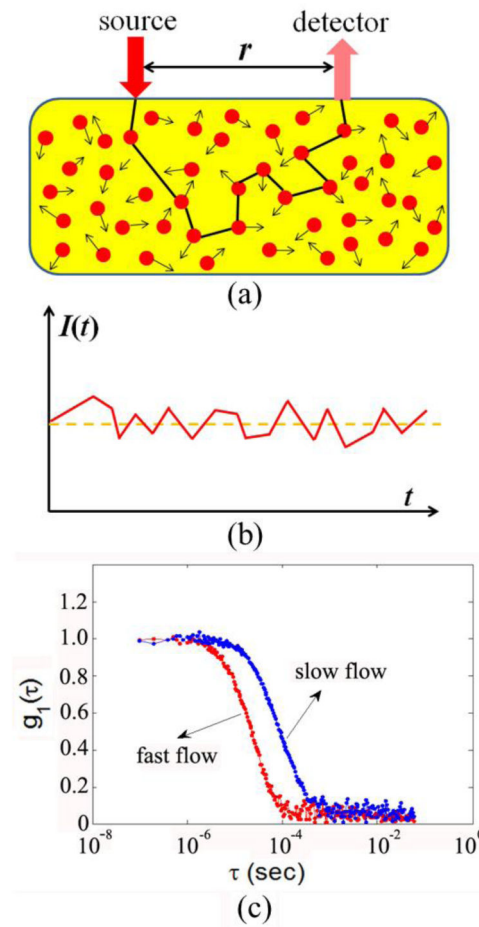
Fig. 1.
The principle of diffuse correlation spectroscopy (DCS) for blood flow measurements in deep/thick tissues. (**a**) Source and detector fibers are placed on the tissue surface within a distance of **r** for light delivery and collection; (**b**) Light intensity I(t), detected by the APD, fluctuates with time due to the motions of RBCs; (**c**) Blood flow change can be quantified from the shift of temporal electric field autocorrelation function curves.
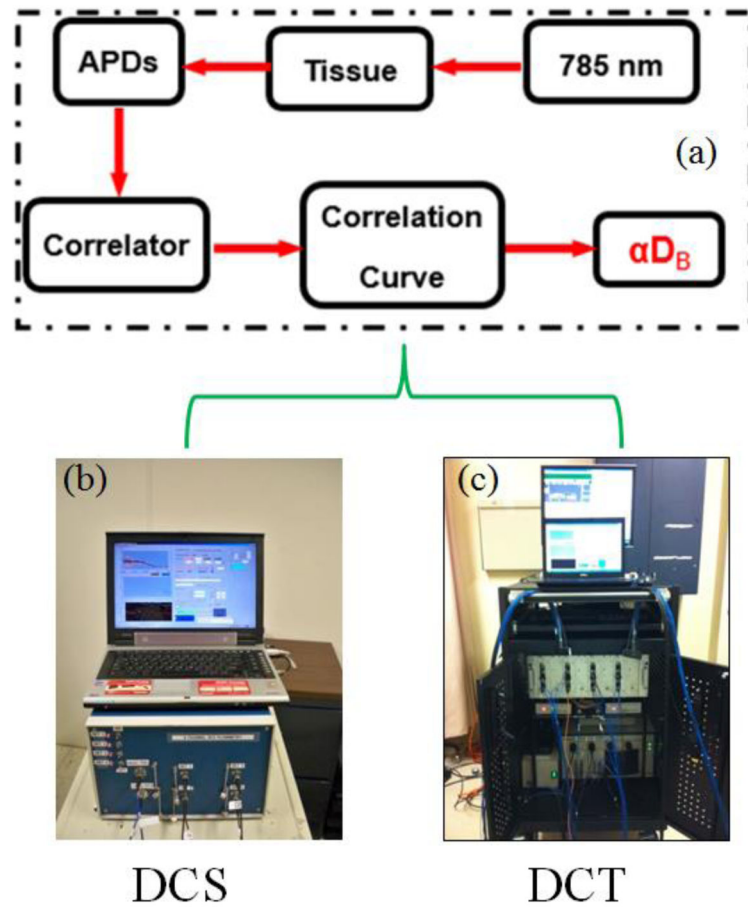
Fig. 2.
The schematic diagram (**a**) and instrument photos of typical DCS (**b**) and DCT (**c**) systems.
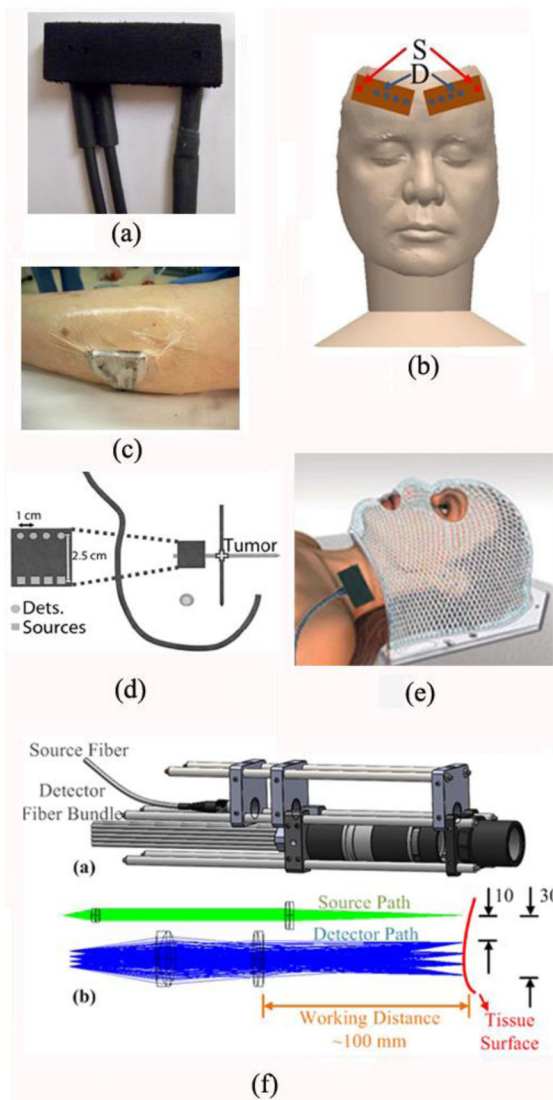
Fig. 3.
A variety of optical probes for DCS/DCT measurements. (**a**) A typical DCS probe consisting of source and detector fibers; (**b**) Two DCS probes taped on both sides of a frontal head for cerebral blood flow measurements; (**c**) A DCS probe taped on top of the calf muscle; (**d**) A hand-held DCS probe scanning over a breast tumor; (**e**) A DCS probe placed on top of the head/neck tumor; (**f**) A noncontact DCS probe with lens system focusing the source and detectors on the surface of tissue. Some of the figures are reproduced from the subfigures in the references (Huang *et al.*, 2015c; Durduran *et al.*, 2005)
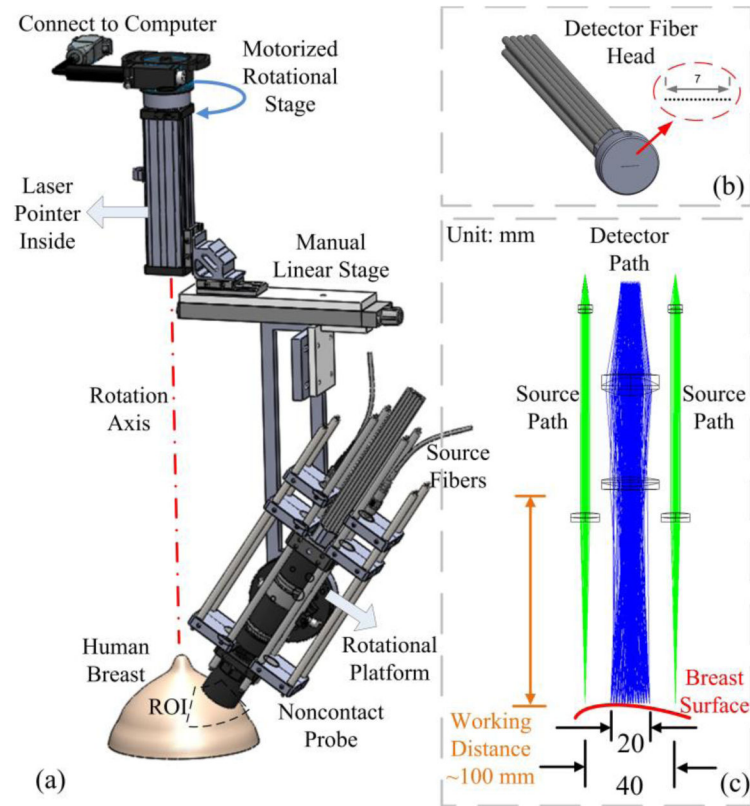
Fig. 4.
A noncontact DCT probe with rotational scanning system. **(a)** Noncontact DCT probe head was scanned over a region of interest (ROI) on the breast by a motorized rotational stage, **(b)** A linear array of single-mode detector fibers, **(c)** Source and detector fibers were projected on the breast surface using achromatic lenses; two source paths were attached to the sides of the detector path. This figure is reproduced from Fig. 1 in the reference (Huang *et al.*, 2015b).
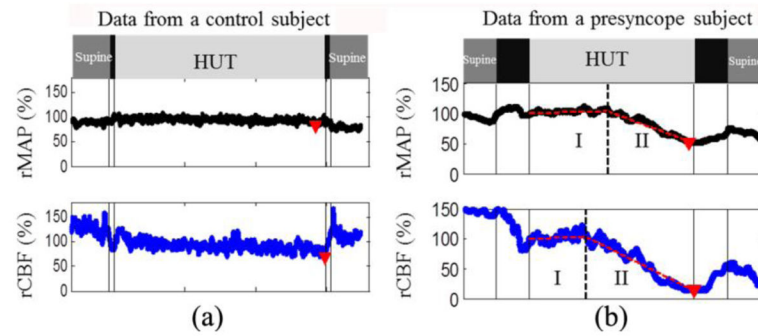
Fig. 5.
Relative changes in mean artery blood pressure (rMAP) and cerebral blood flow (rCBF) from a control subject **(a)** and a presyncope subject **(b)** during Head-Up-Tilting (HUT). The solid vertical lines indicate the beginning or ending of tilting up and tilting down. The triangles indicate the minima of rMAP and rCBF during HUT. The two connected dashed lines on top of the raw data **(b)** demonstrate the two-line fitting results. The dashed vertical lines indicate the break-points separating Stage I and Stage II. This figure is reproduced from the subfigures of Fig. 1 in the reference (Cheng *et al.*, 2014).
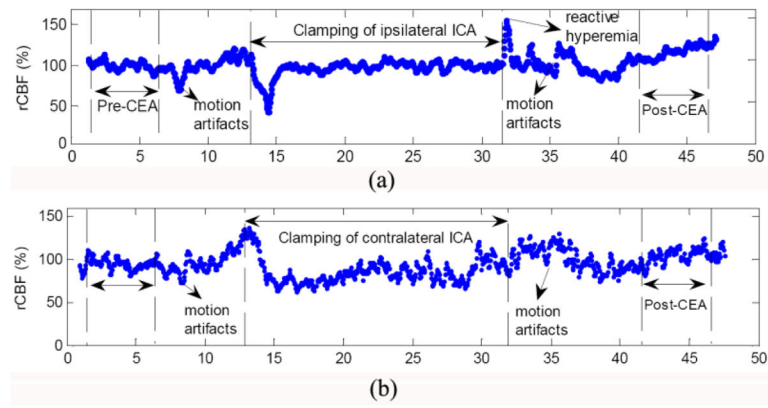
Fig. 6.
Typical relative changes in cerebral blood flow (rCBF) **(a)** at the surgical side (ipsilateral) and **(b)** at the nonsurgical side (contralateral). This figure is reproduced from subfigures of Fig. 2 in the reference (Shang *et al.*, 2011b).
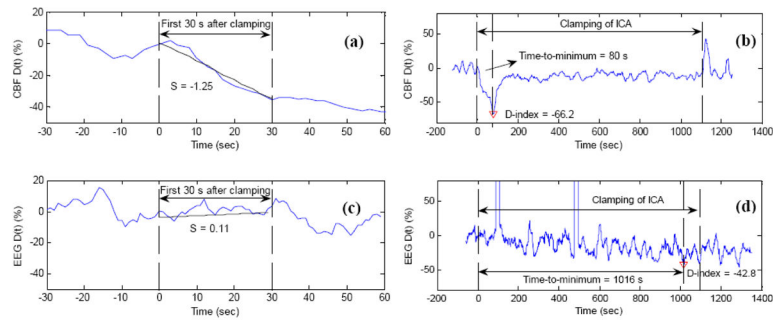
Fig. 7.

Comparison of DCS and EEG measurement results in a typical patient during carotid endarterectomy (CEA) when the internal carotid artery (ICA) was temporarily clamped. The resulted ischemic status by the ICA clamping was characterized by the slope (S), D-index, and time-to-minimum for both CBF (top panel) and EEG (bottom panel) at the surgical side. Here the slope (S) is the deceasing rate of variable $D(t)$ during the first 30-second clamping period, and $D(t)$ represents the percentage change of variable (CBF or EEG spectral power) at time t, when compared to pre-clamping baseline. The minimum of $D(t)$ during the entire period of clamping is defined as D-index, representing the most severe cerebral hypoperfusion during ICA clamping. The period from the beginning of clamping to the time of $D(t)$ attaining its minimum (D-index) is defined as time-to-minimum. The large negative CBF slope (S = −1.25) during the first 30-second clamping period indicates the rapid CBF decrease due to ICA clamping (**a**). The time duration of CBF decrease and maximal CBF decrease during the entire clamping period were characterized by time-to-minimum (80 s) and D-index (−66.2%), respectively (**b**). By contrast, the EEG power changes were small and slow (S = 0.11) (**c**), and reached its minimum (D-index = −42.8%) in a long period of time (time-to-minimum = 1016 s) (**d**). This figure is reproduced from Fig. 4 in the reference (Shang *et al.*, 2011b).
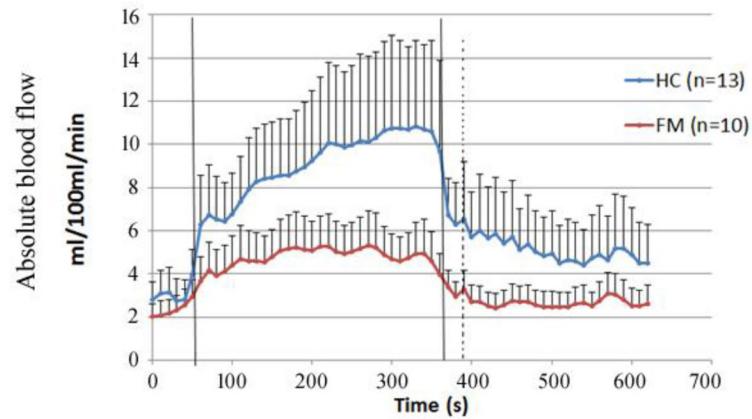
Fig. 8.
Average absolute blood flow responses to handgrip exercise in 10 subjects with fibromyalgia (FM) and 13 age-matched healthy controls (HC). The vertical lines indicate the beginning and end of exercise. Average pre-exercise blood flow value, determined as the average of data points 30 s before the onset of exercise, was 3.19 ± 1.03 ml/100 ml/min for the healthy subjects and 2.63 ± 0.71 ml/100 ml/min for the FM subjects ($p = 0.444$). Plateau blood flow value, determined as the average of points 30 s before the end of exercise was 10.71 ± 3.91 ml/100 ml/min for healthy subjects and 4.83 ± 1.42 ml/100 ml/min for FM subjects ($p = 0.018$).
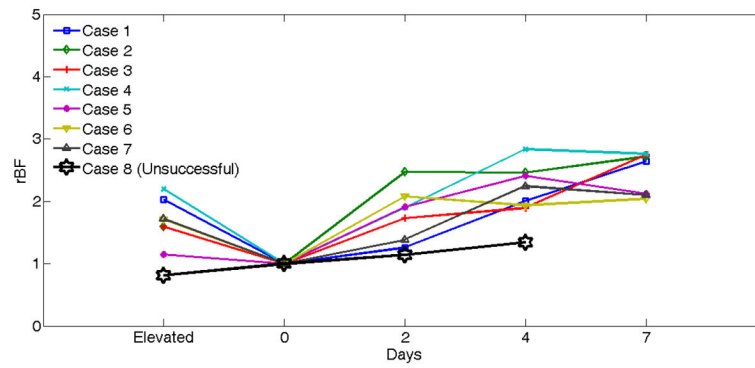
Fig. 9.

Comparison of rBF changes between seven successful and one unsuccessful flaps. The rBF values over the seven successful cases (Cases 1 to 8) during operation and on postoperative days 2, 4, 7 are presented individually. rBF from the unsuccessful flap case (Case 8) was measured at the time of flap elevation and on postoperative days 2 and 4. The data from the unsuccessful case (Case 8) at Day 7 are not available due to the subsequent re-flap before that day. This figure is reproduced from Fig. 6 in the reference (Huang *et al.*, 2015c).
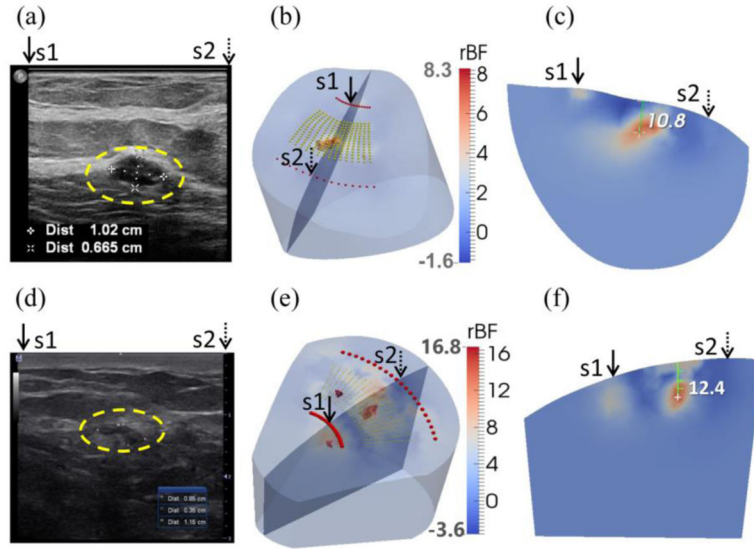
Fig. 10.

Clinical examples of two low-grade carcinomas in situ. (**a**) Ultrasound image of breast with a tumor (inside the yellow dashed circle) in the first patient. The tumor mass center is located at 19.2 mm beneath the skin surface. (**d**) Ultrasound image of breast with a tumor (inside the yellow dashed circle) in the second patient. The tumor mass center is located at 13.3 mm beneath the skin surface. (**b**) and (**e**) show the reconstructed 3-D tumor blood flow contrasts imaged by the ncDCT in the first and second patients, respectively. For the comparison of ultrasound and ncDCT results, an ultrasound imaging plane along the transducer line and across the overlapped two specific light sources (S1 and S2) of ncDCT (see Fig. 4) is presented in the 3-D reconstructed image. The backgrounds are presented with 30% transparency of the original color clarity. (**c**) and (**f**) show the cross-section views through the reconstructed tumor centers, which can be directly compared to the 2-D ultrasound tumor images [(**a**) and (**d**)], respectively. This figure is reproduced from Fig. 8 in the reference (He *et al.*, 2015).
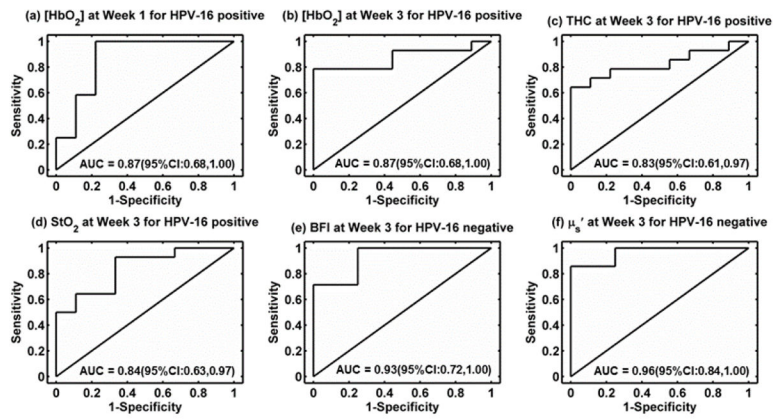
Fig. 11.
Receiver operating characteristic curves (ROC) and the associated areas under the curve (AUC) for discriminating tumors with incomplete response (IR) or complete response (CR). (**a, b**) [HbO$_2$] at Week 1 and Week 3 in HPV-16 positive patients, (**c**) THC at Week 3 in HPV-16 positive patients, (**d**) StO$_2$ at Week 3 in HPV-16 positive patients, (**e**) BFI in HPV-16 negative patients at Week 3, and (**f**) μ_s' in HPV-16 negative patients at Week 3. This figure is reproduced from Fig. 5 in the reference (Dong *et al.*, 2016).